Chemical Geology 330–331 (2012) 86–100

Contents lists available at SciVerse ScienceDirect

Chemical Geology

journal homepage: www.elsevier.com/locate/chemgeo

Reaction path modeling of enhanced *in situ* CO_2 mineralization for carbon sequestration in the peridotite of the Samail Ophiolite, Sultanate of Oman

Amelia N. Paukert [a,*], Jürg M. Matter [a], Peter B. Kelemen [a], Everett L. Shock [b,c], Jeff R. Havig [b]

[a] Lamont-Doherty Earth Observatory, Columbia University, 61 Route 9W, Palisades, NY 10964, United States
[b] School of Earth & Space Exploration, Arizona State University, P.O. Box 871404, Tempe, AZ 85287–1404, United States
[c] Department of Chemistry & Biochemistry, Arizona State University, Tempe, AZ 85287, United States

ARTICLE INFO

Article history:
Received 5 January 2012
Received in revised form 16 July 2012
Accepted 13 August 2012
Available online 24 August 2012

Editor: B. Sherwood Lollar

Keywords:
CO_2-water-rock interaction
Mineral carbonation
In situ CO_2 mineralization
Geochemical modeling
Geologic CO_2 storage

ABSTRACT

The peridotite section of the Samail Ophiolite in the Sultanate of Oman offers insight into the feasibility of mineral carbonation for engineered, *in situ* geological CO_2 storage in mantle peridotites. Naturally occurring CO_2 sequestration via mineral carbonation is well-developed in the peridotite; however, the natural process captures and sequesters CO_2 too slowly to significantly impact the concentration of CO_2 in the atmosphere. A reaction path model was developed to simulate *in situ* CO_2 mineralization through carbonation of fresh peridotite, with its composition based on that of mantle peridotite in the Samail Ophiolite and including dissolution kinetics for primary minerals. The model employs a two-stage technique, beginning with an open system and progressing to three different closed system scenarios- a natural system at 30 °C, an engineered CO_2 injection scenario at 30 °C, and an engineered CO_2 injection scenario at 90 °C. The natural system model reproduces measured aqueous solute concentrations in the target water, signifying the model is a close approximation of the natural process. Natural system model results suggest that the open system achieves steady state within a few decades, while the closed system may take up to 6,500 years to reach observed fluid compositions. The model also identifies the supply of dissolved inorganic carbon as the limiting factor for natural CO_2 mineralization in the deep subsurface. Engineered system models indicate that injecting CO_2 at depth could enhance the rate of CO_2 mineralization by a factor of over 16,000. CO_2 injection could also increase mineralization efficiency – kilograms of CO_2 sequestered per kilogram of peridotite – by a factor of over 350. These model estimates do not include the effects of precipitation kinetics or changes in permeability and reactive surface area due to secondary mineral precipitation. Nonetheless, the faster rate of mineralization in the CO_2 injection models implies that enhanced *in situ* peridotite carbonation could be a significant sink for atmospheric CO_2.

1. Introduction

Recently, greater attention has been given to carbon capture and storage (CCS) in geologic formations as a method for helping prevent the rise of CO_2 in the atmosphere and ensuing global climate change. In 2010, geologic CCS was added to the list of Kyoto Protocol clean development mechanisms, making it more important than ever to characterize the various methods of geologic storage. Injection into saline aquifers and depleted oil and gas reservoirs are accepted, conventional approaches to geologic storage (Benson et al., 2005). For the past 15 years, Statoil has been capturing CO_2 in natural gas extracted from the North Sea and injecting it back into the Utsira Sand formation above the Sleipner West gas field at a rate of 1 Mton CO_2/year (e.g., Chadwick et al., 2004; Holloway, 2005). CO_2 sequestration by mineral carbonation in mafic and ultramafic rocks, first proposed in the 1990s (e.g., Seifritz, 1990), is now also being considered as a form of geologic storage since it offers permanent and safe sequestration of CO_2 as carbonate minerals (e.g., reviews in Matter and Kelemen, 2009; Kelemen et al., 2011).

Both basalt and peridotite have been suggested as host formations for *in situ* mineralization (e.g., McGrail et al., 2006; Matter et al., 2007; Oelkers et al., 2008; Kelemen and Matter, 2008). Peridotite is thought to have the benefit of faster carbonation rates, while continental basalt formations are thought to be more permeable and porous, which results in higher injectivity and the possibility of pore space storage of CO_2 in supercritical or dissolved forms as well as in carbonate minerals.

Lab experiments suggest that in freshwater solutions, carbonation rates of peridotite are much faster than basalt due to the high concentration of olivine: at the pH and temperature relevant for *in situ* CO_2 mineralization (pH 3 and 90 °C), the rate of olivine dissolution is two orders of magnitude faster than that of crystalline basalt (Palandri and Kharaka, 2004; Schaef and McGrail, 2009). However, when the solution is seawater, peridotite dissolution may only be about twice as fast as basalt dissolution (Wolff-Boenisch et al., 2011). Experiments involving

* Corresponding author at: Lamont-Doherty Earth Observatory, 61 Route 9W, Comer Bldg 417, Palisades, NY 10964, United States. Tel.: +1 845 365 8652.
E-mail address: APaukert@LDEO.Columbia.edu (A.N. Paukert).

0009-2541/$ – see front matter © 2012 Elsevier B.V. All rights reserved.
http://dx.doi.org/10.1016/j.chemgeo.2012.08.013

the whole olivine carbonation process, rather than just dissolution, have shown that by using a $Na^+ - HCO_3^-$ solution the rate of carbonation can be enhanced by a factor of 4 and extent of carbonation more than doubled, compared to $Na^+ - Cl^-$ solutions (O'Connor et al., 2004; Chizmeshya et al., 2007). The effect of such solutions on basalt carbonation has not yet been extensively studied.

Flood basalts may be structurally favorable for CO_2 injection due to their higher porosity and permeability. Comparing representative sites, such as vesicular basalt from the Cascade Range in Oregon and peridotite of the Samail Ophiolite in Oman, shows that the permeability of basalt can range from equal to that of fractured peridotite (~10 millidarcies) to up to 3 orders of magnitude higher (Saar and Manga, 1999; Dewandel et al., 2005), though these numbers are site specific. In addition, flood basalts often have a layer-cake structure that could help store CO_2 within the formation, consisting of brecciated flow tops, which have good injectivity and storage capacity, alternating with massive flow interiors, which act as an impermeable cap rock to upward CO_2 migration (McGrail et al., 2006).

Before preference is given to either rock type, our understanding of the mineralization process would benefit from further examination of both its kinetics and thermodynamics. For instance, *in situ* mineralization has been considered too slow to be a viable option for sequestering sufficient amounts of CO_2 (e.g., Mazzotti et al., 2005). However, recent studies suggest mineralization may be faster than previously thought (O'Connor et al., 2004; Chizmeshya et al., 2007), and consequently *in situ* mineralization deserves more investigation (Matter and Kelemen, 2009). The rates for *in situ* mineralization need to be determined through field scale studies. While a number of laboratory experiments have been conducted on dissolution of basalt (e.g., Gislason and Eugster, 1987; McGrail et al., 2006; Schaef and McGrail, 2009) and olivine, the primary mineral of peridotite (e.g., Oelkers, 2001; Giammar et al., 2005; Hänchen et al., 2006), there is often a discrepancy between laboratory and field scale rates. These differences may be attributable to disparities between lab conditions and field conditions with respect to reactive surface area, permeability, and mineral/fluid ratios (White and Brantley, 2003). Thus, in order to accurately predict timescales for *in situ* mineralization, *in situ* rates must be better constrained.

The thermodynamic properties of relevant minerals and aqueous species also require further scrutiny. The thermodynamic database developed at Lawrence Livermore National Lab that is often used in reaction path modeling is extensive, but not all-encompassing. Studies focusing on particular species often involve updating the thermodynamic database for those species at the temperature and pressure of the study, as Gysi and Stefansson (2011) did for carbonates, zeolites, phyllosilicates, and other secondary minerals involved in basalt carbonation, and McCollom and Bach (2009) did for Mg–Fe solid solutions of serpentine, talc, brucite, pyroxenes, and amphibole in serpentinization (hydration) of peridotite. Incomplete or disparate thermodynamic databases make it difficult to directly compare modeling studies conducted by different groups. A universal database could help to evaluate the effectiveness of CO_2 mineralization in basalt and peridotite.

There are several open questions relating to *in situ* mineralization that should be answered in order to assess its potential as a method of CO_2 sequestration. These include:

- What are the timescales associated with natural and engineered *in situ* CO_2 mineralization?
- What are the limiting factors in natural and engineered *in situ* CO_2 mineralization?
- Could the process be enhanced to make CO_2 uptake fast enough to have a significant impact on atmospheric CO_2 concentration?

This paper aims to address some aspects of these questions as they relate to peridotite carbonation by focusing on the ongoing natural CO_2 mineralization in the Samail Ophiolite as a natural analog for an engineered CO_2 injection process.

2. Geological setting and groundwater evolution

The peridotite aquifer of the Samail Ophiolite in the Sultanate of Oman is a site of exceptionally well-developed naturally occurring *in situ* CO_2 mineralization. The Samail Ophiolite is the largest ophiolite in the world, with over 15,000 km^3 of peridotite in the upper few kilometers of the mantle section (Nicolas et al., 2000; Kelemen and Matter, 2008). The mantle peridotite consists of approximately 74% partially serpentinized olivine, 24% orthopyroxene, 2% spinel, and trace amounts of clinopyroxene (Boudier and Coleman, 1981).

Natural *in situ* mineral carbonation proceeds in the following manner, illustrated by Fig. 1 (Barnes and O'Neil, 1969; Neal and Stanger, 1985; Bruni et al., 2002; Hansen et al., 2005; Kelemen and Matter, 2008): surface water infiltrates shallow aquifers where it reacts with peridotite in an open system with atmospheric levels of CO_2 and O_2, increasing dissolved Mg^{2+}, Ca^{2+}, Si^{4+}, and CO_2 (Eq. (1)).

$$Mg_2SiO_4 + 4CO_2 + 2H_2O \rightarrow 2Mg^{2+} + 4HCO_3^- + SiO_2 \quad (1)$$

At the same time, interaction with soil CO_2 and carbonate rocks or carbonate dust further increases dissolved Ca^{2+} and CO_2. This results in a $Mg^{2+} - HCO_3^-$ water, often referred to as Type I. This Type I water then infiltrates to a depth where it can no longer communicate with the atmosphere and is thus cut off from its source of inorganic carbon. In this closed system, the water continues to react with peridotite and precipitates serpentine, brucite, magnesite and dolomite. Through this open and closed system reaction path, both Mg^{2+} and Ca^{2+} are released from the peridotite, but Mg^{2+} preferentially goes into secondary minerals, such as chrysotile and brucite, while Ca^{2+} is left to accumulate in the water (Eq. (2)).

$$4Mg_2SiO_4 + CaMgSi_2O_6 + 7H_2O \rightarrow 3Mg_3Si_2O_5(OH)_4 + Ca^{2+} + 2OH \quad (2)$$

The dissolution reactions also consume protons, raising the pH as high as 12. This results in an alkaline $Ca^{2+} - OH^-$ groundwater with virtually no Mg^{2+} or dissolved inorganic carbon (DIC), often called Type II water. When this water reaches the near-surface or discharges at the surface in the form of alkaline springs, it undergoes either air-water interaction or mixing with shallow groundwater or surface water. Air-water interaction allows the absorption of CO_2 directly from the atmosphere and results in the formation of Ca-rich carbonates (Eq. (3a)), while mixing of Type II water with Type I water causes the precipitation of Ca-rich carbonates and brucite (Eqs. (3a) and (3b)). In both scenarios, carbonate formation lowers the pH to basic levels (pH 8–9).

$$Ca^{2+} + 2OH^- + CO_2 \rightarrow CaCO_3 + H_2O \quad (3a)$$

$$Mg^{2+} + 2OH^- \rightarrow Mg(OH)_2 \quad (3b)$$

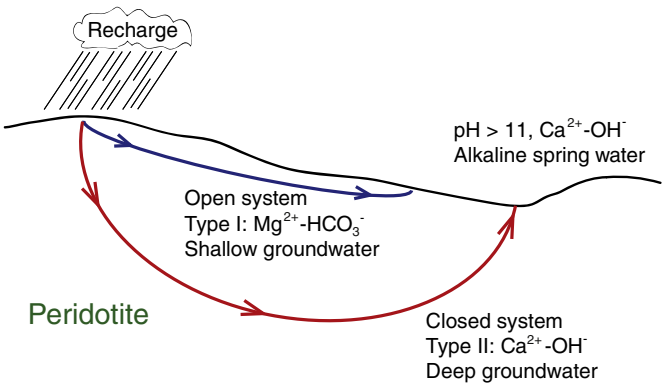

Fig. 1. Flowpath schematic illustrating groundwater evolution in the peridotite aquifers of the Samail Ophiolite, modified from Neal and Stanger (1985).

Overall, the system forms abundant carbonate minerals, both in the subsurface and in surficial travertine terraces, and thus sequesters CO_2. In the mantle peridotite alone, up to 10^5 tons of CO_2 are converted to solid carbonate minerals each year (Kelemen and Matter, 2008; Kelemen et al., 2011).

In Oman, unlike other alkaline spring localities such as California or Italy, Type II spring waters also have elevated Na^+ and Cl^- concentrations relative to surface and shallow groundwater (Barnes and O'Neil, 1969; Neal and Stanger, 1985; Bruni et al., 2002). The excess Na^+ and Cl^- likely come from leaching of sea salts adsorbed onto mineral surfaces, or salty fluids in micropores or intracrystalline inclusions in the formation residual from when the ophiolite was submerged under the sea (Neal and Stanger, 1985; Orberger et al., 1990; Sharp and Barnes, 2004; Dewandel et al., 2005).

3. Analytical methods

3.1. Field methods

In January 2009 and 2010, 51 water samples were collected from 13 sites: 10 alkaline spring sites and 3 wells set in peridotite (Fig. 2). Water sampling locations included alkaline springs where they discharged from peridotite, the surface flowpath of these alkaline waters (including areas of mixing with surface waters), nearby wadis (stream beds, often with ephemeral water flow), afalaj (irrigation channels), and shallow wells in peridotite.

Water samples were collected in new or triple rinsed syringes and filtered using sterile Acrodisc 0.8/0.2 µm syringe filters with supor membranes into new polyethylene bottles. Samples for measuring

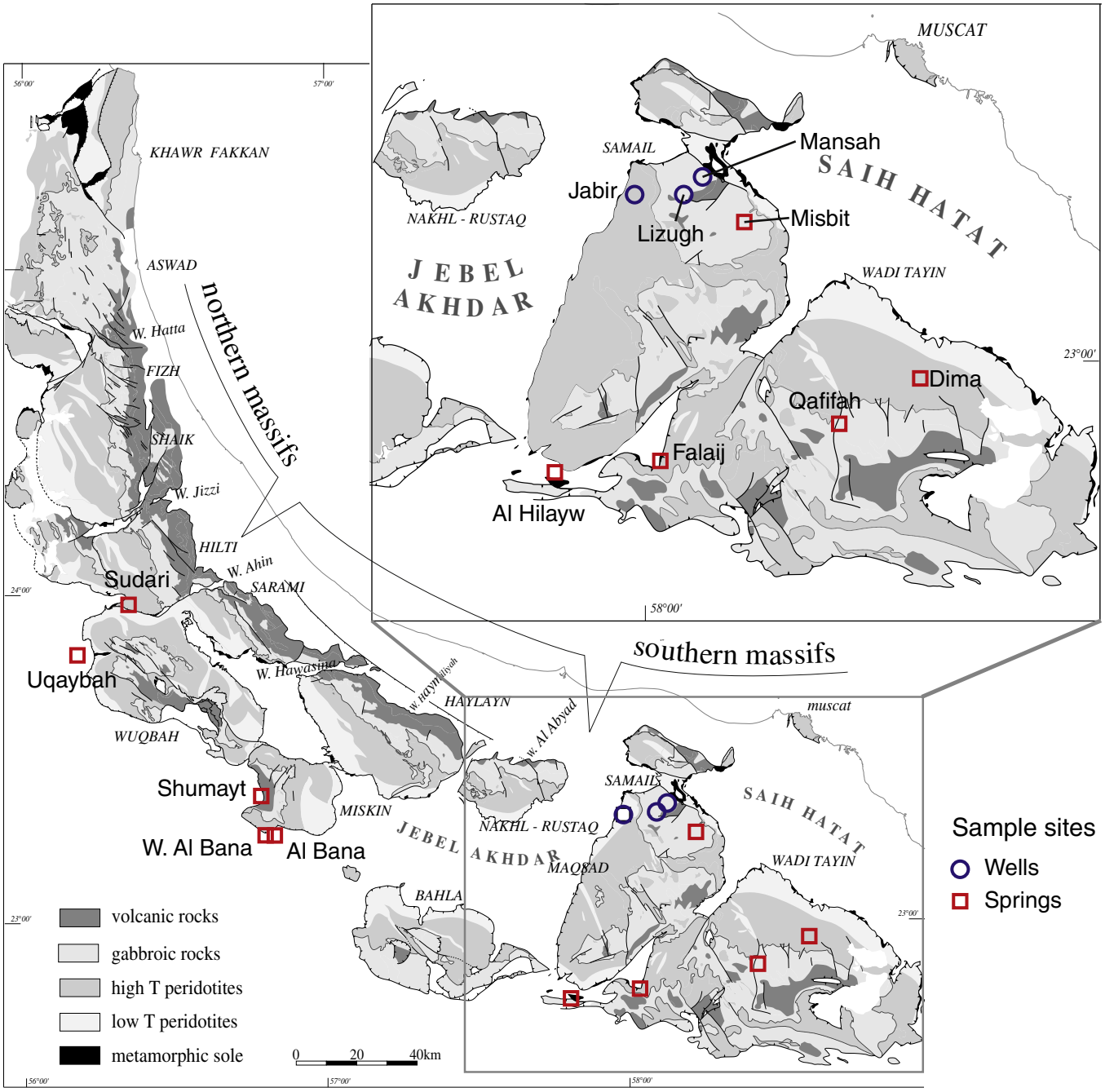

Fig. 2. Geologic map of the Samail Ophiolite, northern and southern massifs, from Nicolas et al. (2000) showing sample site locations.

major cations and trace elements were acidified in the field with concentrated HNO_3. At the sample sites, pH, temperature, conductivity, and oxidation-reduction potential were measured using a WTW Multi 3400i multi-parameter field meter. Alkalinity was measured in the field with a Hach 16900 Digital Titrator using a two-step titration process which isolates carbonate alkalinity from hydroxide alkalinity.

Additionally, 19 mineral samples were collected from 3 of the alkaline spring sites. The samples were taken from areas of active precipitation or deposition at or near spring discharge areas, including crystalline films atop alkaline spring pools, white floc from the bottom of pools, and deposits forming rippled terraces in areas of faster water flow, such as on steeper slopes. Mineral samples were collected in new, sterile, polyethylene sample bags.

3.2. Laboratory methods

Major anions (Cl^-, NO_3^-, SO_4^{2-}, NO_2^-, PO_4^{3-}, Br^-, F^-) were analyzed by ion chromatography on a Dionex IC2000 with an AS18 column. Major cations (Ca^{2+}, Na^+, K^+, Mg^{2+}, Si^{4+}) were analyzed using inductively coupled plasma atomic emission spectrometry (ICP-AES) on an

Table 1
Field data for water samples.

Sample ID	Location	UTM Coord. (WGS-84)		pH	Temp °C	Cond. µS/cm	ORP mV
		Easting	Northing				
Alkaline spring outlets							
OM10_01A	Misbit	0625997	2576261	11.20	31.6	1640	−404
OM10_02L	Falaij	0608436	2525957	11.52	30.8	2230	−393
OM10_03R	Falaij	0608561	2526486	11.63	27.9	1967	−390
OM10_04S	Qafifah	0646115	2533648	11.76	22.4	1685	−247
OM10_04U	Qafifah	0646071	2533679	11.71	24.9	1778	−611
OM10_05AA	West of Al Bana	0487584	2575976	11.65	28.5	3400	−324
OM10_05AD	West of Al Bana	0487338	2576123	11.68	32.6	3420	−393
OM10_05AF	West of Al Bana	0487951	2575513	11.90	24.2	2850	−436
OM10_07AJ	Shumayt	0486044	2588467	11.46	33.4	1782	−231
OM10_08AM	Shumayt	0486041	2588458	11.53	31.5	1772	−323
OM10_09AT	Sudari	0443118	2650087	11.61	30.4	1893	−292
OM10_10AV	Uqaybah	0426225	2633900	11.61	21.4	1442	−200
OM09_W04F	Al Hilayw	0585875	2523231	11.59	26.3	2250	−247
OM09_W04G	Al Hilayw	0585877	2523246	11.60	27.1	2230	−220
OM09_W05L	Qafifah	0646070	2533683	11.64	23.8	1854	−338
OM09_W06O	Dima	0663442	2542614	11.45	30.3	1905	−369
OM09_W13F	Shumayt	0486044	2588467	11.50	28.1	1770	−495
Alkaline water along surface flowpath							
OM10_01B	Misbit	0625971	2576256	11.26	30.5	1641	−322
OM10_02J	Falaij	0608427	2525980	11.63	28.2	2200	−283
OM10_02K	Falaij	0608431	2525972	11.60	26.8	2210	−296
OM10_03P	Falaij	0608553	2526473	11.49	23.3	1507	−133
OM10_03Q	Falaij	0608557	2526477	11.60	22.9	1752	−247
OM10_05AB	West of Al Bana	0487580	2575969	11.74	25.4	2770	−280
OM10_06AG	Al Bana	0489557	2575443	11.14	37.7	1421	−434
OM10_06AH	Al Bana	0489564	2575430	11.16	38.4	1537	−645
OM09_W04I	Al Hilayw	0585880	2523239	11.72	20.7	2200	50
OM09_W10V	Misbit	0625966	2576248	11.21	30.6	1616	−379
Mixed spring and wadi water							
OM10_01C	Misbit	0625974	2576257	8.95	19.8	794	NA
OM10_01E	Misbit	0625938	2576240	10.20	27.1	875	−262
OM10_04V	Qafifah	0646071	2533676	11.16	23.7	904	−208
OM10_04W	Qafifah	0646072	2533675	10.27	20.8	696	−128
OM10_04X	Qafifah	0646074	2533666	8.94	23.3	664	53
OM10_04Y	Qafifah	0646073	2533671	11.91	20.5	1820	−75
OM10_05AC	West of Al Bana	0487574	2575966	11.55	16.5	1873	30
OM10_05AE	West of Al Bana	0487304	2576112	11.87	20.3	2790	−166
OM10_08AN	Shumayt	0486037	2588460	10.18	28.6	720	NA
OM10_08AO	Shumayt	0486021	2588453	10.43	27.4	734	NA
OM10_09AS	Sudari	0443119	2650088	11.27	18.2	1013	−195
OM10_09AU	Sudari	0443117	2650082	11.56	20.1	1258	−235
OM10_10AW	Uqaybah	0426225	2633900	8.49	17.5	911	145
OM09_W06N	Dima	0663452	2542655	9.92	17.5	864	−41
Shallow groundwater							
OM10_06AI	Al Bana	0489581	2575531	8.52	29.0	467	NA
OM10_12AZ	Jabir	0602847	2582068	9.36	34.1	586	94
OM10_13BA	Lizugh	0612902	2582098	7.77	33.9	968	147
OM10_15BC	Trib. to Mansah	0616917	2585510	7.90	34.5	902	120
OM09_W08S	Qafifah	0646196	2533635	8.99	21.6	493	NA
Fresh surface water							
OM10_01D	Misbit	0626252	2576472	8.35	25.2	786	41
OM10_08AP	Shumayt	0486065	2588470	7.90	27.0	723	NA
OM10_09AR	Sudari	0443057	2650131	8.76	21.5	923	211
OM09_W06P	Dima	0663430	2542608	8.12	20.2	973	182
OM09_W12B	Sudari	0443056	2650128	8.16	17.1	1440	187

Horiba Jobin-Yvon Activa M with PFA nebulizer. Trace elements and DIC were measured at Arizona State University using an inductively coupled plasma mass spectrometer and an OI Analytical Model 1010 Wet Oxidation TOC Analyzer, respectively. The analytical accuracy of major cation analysis was ± 3%, measured as variation from NIST Standard Reference Material 1640a-Trace Elements in Natural Water. The analytical precision of major cation and anion analysis was better than 1.5% and 4% relative standard deviation at 1σ, respectively. All but a few samples have a charge balance within ± 5% electroneutrality.

The collected mineral samples were dried in an oven at 40 °C and crumbled to a fine powder. The powdered sample was then analyzed by x-ray diffraction using an Inel XRG 3000 diffractometer and interpreted using MAUD software v. 2.26 (Lutterotti et al., 1997) to semi-quantitatively estimate mineral composition.

Table 2
Major ion chemistry and trace elments for water samples[a].

Sample ID	Cl^-	NO_3^-	SO_4^{2-}	DIC	OH^- [c]	Ca^{2+}	Na^+	K^+	Mg^{2+} [d]	Si^{4+}	Al^{3+} [e]	Fe^{2+} [e]
Alkaline spring outlets												
OM10_01A	6.97	<0.01	0.07	0.11	3.28	2.12	6.54	0.15	1.65E−02	0.04	2.26E−02	5.19E−05
OM10_02L	8.19	<0.01	0.01	0.07	5.44	1.83	9.63	0.26	2.47E−02	<0.02	<5 E−04	4.83E−05
OM10_03R	7.49	<0.01	0.03	0.06	4.84	1.67	8.14	0.22	3.70E−02	<0.02	<5 E−04	<2 E−05
OM10_04S	5.11	<0.01	0.01	0.10	4.48	1.75	6.55	0.16	1.89E−02	<0.02	6.30E−04	4.17E−05
OM10_04U	4.78	<0.01	0.01	0.12	4.68	1.69	6.25	0.14	1.89E−02	<0.02	<5 E−04	<2 E−05
OM10_05AA	11.38	<0.01	0.01	0.04	6.08	1.66	13.81	0.31	3.00E−02	<0.02	<5 E−04	3.76E−05
OM10_05AD	12.52	<0.01	0.01	0.05	8.52	2.11	16.78	0.33	3.29E−02	<0.02	<5 E−04	3.94E−05
OM10_05AF	10.51	<0.01	0.01	0.10	6.90	1.57	13.82	0.26	2.67E−02	<0.02	<5 E−04	1.50E−04
OM10_07AJ	5.28	<0.01	<0.005	0.05	5.04	1.87	6.53	0.15	2.10E−02	<0.02	<5 E−04	3.58E−05
OM10_08AM	5.26	<0.01	<0.005	0.04	4.86	1.85	6.45	0.15	1.89E−02	<0.02	<5 E−04	<2 E−05
OM10_09AT	5.91	<0.01	0.01	0.04	4.74	1.78	7.56	0.17	1.93E−02	<0.02	5.82E−04	5.91E−05
OM10_10AV	6.55	<0.01	0.07	0.14[b]	2.52	2.56	4.28	0.15	4.65E−03	<0.02	<5 E−04	<2 E−05
OM09_W04F	8.33	0.01	0.04	0.22[b]	4.78	1.40	11.08	0.25	8.64E−03	0.09	5.41E−03	8.42E−05
OM09_W04G	8.22	<0.01	0.03	0.02[b]	5.22	1.31	10.91	0.26	9.05E−03	0.11	5.41E−03	4.01E−05
OM09_W05L	4.67	0.01	0.01	0.38[b]	4.40	1.66	6.19	0.19	6.50E−02	0.06	1.56E−02	1.74E−03
OM09_W06O	6.73	<0.01	0.01	0.16[b]	4.74	1.82	7.93	0.23	7.24E−03	0.04	4.41E−03	4.05E−05
OM09_W13F	4.96	<0.01	0.01	0.20[b]	4.34	1.82	6.56	0.16	7.15E−03	0.06	5.97E−03	1.04E−04
Alkaline water along surface flowpath												
OM10_01B	7.06	<0.01	0.07	0.11	3.18	1.85	6.54	0.15	2.30E−02	0.05	2.33E−02	4.83E−05
OM10_02J	8.10	<0.01	0.01	0.05	5.22	2.10	9.57	0.25	2.51E−02	<0.02	<5 E−04	8.77E−05
OM10_02K	8.11	<0.01	0.01	0.07	5.34	1.87	9.63	0.26	2.72E−02	<0.02	<5 E−04	4.12E−05
OM10_03P	6.94	<0.01	0.02	0.06	2.36	0.79	8.57	0.23	1.93E−02	<0.02	<5 E−04	4.30E−05
OM10_03Q	7.21	<0.01	0.03	0.08	3.74	1.03	8.35	0.23	2.63E−02	<0.02	<5 E−04	<2 E−05
OM10_05AB	11.60	<0.01	0.01	0.13	6.10	1.50	14.31	0.33	2.59E−02	<0.02	5.19E−04	3.76E−05
OM10_06AG	5.31	<0.01	<0.005	0.04	3.18	1.54	5.52	0.16	9.42E−03	<0.02	<5 E−04	<2 E−05
OM10_06AH	5.47	<0.01	<0.005	0.05	3.72	2.01	6.14	0.16	1.81E−02	<0.02	<5 E−04	4.12E−05
OM09_W04I	8.64	0.01	0.04	0.20[b]	4.22	1.07	11.31	0.28	9.71E−03	0.07	6.67E−03	4.83E−05
OM09_W10V	6.55	<0.01	0.06	0.34[b]	2.66	2.05	6.26	0.10	3.04E−02	0.10	2.30E−02	5.12E−05
Mixed spring and wadi water												
OM10_01C	3.15	0.22	0.72	1.93	0	0.75	3.23	0.10	1.66	0.36	2.19E−03	<2 E−05
OM10_01E	4.59	0.17	0.51	0.68	0	1.22	4.65	0.11	0.98	0.26	6.67E−03	2.51E−05
OM10_04V	3.99	0.01	0.11	0.66	0.92	0.51	5.10	0.11	0.43	0.06	<5 E−04	<2 E−05
OM10_04W	3.18	0.02	0.20	1.93	0	0.27	3.77	0.08	1.21	0.15	<5 E−04	<2 E−05
OM10_04X	1.56	0.08	0.37	4.49	0	0.41	1.59	0.04	2.44	0.34	<5 E−04	7.88E−05
OM10_04Y	4.42	0.01	0.07	1.40[b]	1.64	1.72	6.31	0.15	0.05	0.03	NA	NA
OM10_05AC	11.00	<0.01	0.11	0.69	1.38	0.30	13.10	0.31	0.27	0.05	<5 E−04	2.33E−05
OM10_05AE	12.71	<0.01	0.01	0.07	5.70	0.60	16.28	0.33	2.43E−02	<0.02	<5 E−04	4.66E−05
OM10_08AN	3.08	0.05	0.39	1.66	0	0.56	3.50	0.12	1.58	0.19	<5 E−04	<2 E−05
OM10_08AO	3.31	0.05	0.35	1.40	0	0.20	3.85	0.12	1.39	0.17	<5 E−04	<2 E−05
OM10_09AS	5.75	0.01	0.21	0.47	0.62	0.25	6.69	0.15	0.32	0.03	<5 E−04	<2 E−05
OM10_09AU	5.85	<0.01	0.15	0.07	1.74	0.68	7.03	0.16	0.18	0.02	<5 E−04	<2 E−05
OM10_10AW	6.95	<0.01	0.14	0.64[b]	0	1.54	4.01	0.15	0.31	0.05	<5 E−04	<2 E−05
OM09_W06N	5.61	0.02	0.20	1.48[b]	0	0.30	5.95	0.16	1.13	0.12	2.71E−03	4.66E−04
Shallow groundwater												
OM10_06AI	1.10	0.13	0.46	2.62	0	0.38	0.75	0.04	1.70	0.24	<5 E−04	<2 E−05
OM10_12AZ	2.05	0.09	0.89	1.42[b]	0	0.05	1.43	0.07	2.23	<0.02	<5 E−04	<2 E−05
OM10_13BA	3.79	0.41	0.94	3.14[b]	0	0.70	3.34	0.09	2.49	0.41	NA	NA
OM10_15BC	4.53	0.29	0.80	2.32[b]	0	1.06	4.11	0.06	1.27	0.36	NA	NA
OM09_W08S	1.88	0.05	0.28	1.90[b]	0	0.20	1.64	0.03	1.19	0.13	1.04E−03	5.01E−05
Fresh surface water												
OM10_01D	2.80	0.28	0.75	3.08	0	0.84	3.00	0.09	1.70	0.39	<5 E−04	<2 E−05
OM10_08AP	1.38	0.12	0.64	5.17	0	0.57	1.06	0.10	2.90	0.35	<5 E−04	<2 E−05
OM10_09AR	4.90	0.01	0.50	3.04	0	0.45	4.94	0.12	1.67	0.10	<5 E−04	2.51E−05
OM09_W06P	5.14	<0.01	0.32	3.46[b]	0	0.49	4.51	0.11	1.99	0.18	2.71E−03	4.66E−04
OM09_W12B	8.61	<0.01	0.68	3.14[b]	0	0.48	8.73	0.16	1.69	0.20	5.86E−03	5.91E−04

[a] All concentrations are in mmol/l.
[b] Indicates DIC values from alkalinity, all others are from carbon analyzer.
[c] OH^- values taken from field alkalinity titrations.
[d] Mg values below 1 ppm (0.04 mmol/l) from ICP-MS, all others are from ICP-AES.
[e] All values from ICP-MS.

4. Analytical results

Field data and the chemical composition of the collected water samples are summarized in Tables 1 and 2. The water samples are subdivided into five different classes on the basis of flowpath: i) alkaline spring outlets, ii) alkaline spring water along a surface flowpath with no mixing, iii) alkaline spring water mixed with surface water, iv) shallow groundwater, and v) fresh surface water. All water sample data fall within the range of compositions previously seen in areas with partially serpentinized and carbonated peridotite (e.g., Barnes and O'Neil, 1969; Neal and Stanger, 1985; Bruni et al., 2002). Alkaline spring waters are of Type II $Ca^{2+}-OH^{-}$ water, with high pH (11 to 12), high Ca^{2+} (1 to 2.5 mmol/l), high Na^{+} and Cl^{-} (4 to 17 mmol/l and 5 to 13 mmol/l, respectively), and virtually no Mg^{2+} (5 to 65 μmol/l) or dissolved inorganic carbon (DIC) (20 to 380 μmol/l). Shallow groundwater samples are of Type I $Mg^{2+}-HCO_3^{-}$ water, with a pH between 7.5 and 9 and high Mg^{2+} (1 to 2.5 mmol/l) and DIC (1 to 3 mmol/l). Surface waters have Mg^{2+} concentrations similar to those in shallow groundwater, and higher DIC (3–5 mmol/l).

Along a surface flowpath, alkaline waters show little change in water chemistry from their spring discharge points, with the exception of Ca^{2+}, which decreases in concentration along the surface flowpath. The drop in Ca^{2+} is attributed to uptake of atmospheric CO_2 and precipitation of calcium carbonate along the flowpath. Alkaline spring waters which have mixed with fresh surface water have intermediate levels of Mg^{2+}, Ca^{2+}, and DIC. However, the concentration of Ca^{2+} in these mixed waters is lower than would be expected based on a mixing line between local surface water and alkaline spring water. For example, at Shumayt, mixed water has 0.6 mmol/l less Ca^{2+} than predicted based on a Cl^{-} mixing line. This suggests precipitation of Ca-rich carbonates from the mixed waters, which is supported by the mineral samples collected from these areas.

Mineral saturation states in samples of alkaline spring water and shallow groundwater from wells and afalaj were calculated using EQ3NR, the speciation-solubility code in EQ3/6, v. 8.0 (Wolery and Jarek, 2003). The saturation states were calculated for each sample using major ion concentrations listed in Tables 1 and 2, then the average for the group was taken for each mineral (Fig. 3). For this paper, saturation states are in the form of chemical affinity to equilibrium with respect to solid phases (kcal/mole). Affinity = RT*ln(Q/K), where Q is the reaction quotient and K is the equilibrium constant of the dissolution reaction for the mineral.

Shallow groundwater samples are saturated with respect to aragonite, calcite, magnesite, and quartz, oversaturated with respect to dolomite and chrysotile, and undersaturated with respect to hydromagnesite, brucite, and magnetite (Fig. 3A). Alkaline spring waters are saturated with respect to Ca-rich carbonates – aragonite, calcite, and dolomite, oversaturated with respect to brucite, chrysotile, and magnetite, and undersaturated with respect to hydromagnesite, magnesite, and quartz (Fig. 3B). Shallow groundwater saturation with respect to Ca-carbonates is expected; in the Samail Ophiolite, alluvial conglomerates cemented with Ca-rich carbonates are common in areas of near-surface groundwater (Burns and Matter, 1995). Alkaline spring water saturation with respect to Ca-rich carbonates also fits field data, which show calcite-dolomite veins in the shallow subsurface in areas near alkaline springs, and surficial calcite-rich travertines around the springs (Neal and Stanger, 1985; Clark and Fontes, 1990; Kelemen and Matter, 2008).

Semi-quantitative analysis of XRD results for mineral samples shows that active precipitation is primarily calcium carbonate (aragonite and/or calcite) with minor amounts of brucite and – in one location – a hydrated Mg carbonate (Table 3). The mineral composition varies with depositional setting. Crystalline films atop alkaline spring pools are pure calcium carbonate. Crystalline films atop pools with mixed alkaline spring water and fresh surface water were 97–99% calcium carbonate and 1–3% brucite. Floc at the bottom of pools was 80-99% calcium carbonate, with 1–20% brucite. Rippled terraces downstream of alkaline spring discharge areas were 93–100% calcium carbonate with 0–7% brucite.

These physical structures and mineral compositions result from two surficial carbonation mechanisms described by Stanger (1986): air–water reactions and water mixing reactions. Our crystalline films and rippled terraces match *Stanger's* Ca-carbonate surface films and drapes that form due to alkaline spring air–water reactions in non-turbulent flow regimes and turbulent flow regimes with vigorous

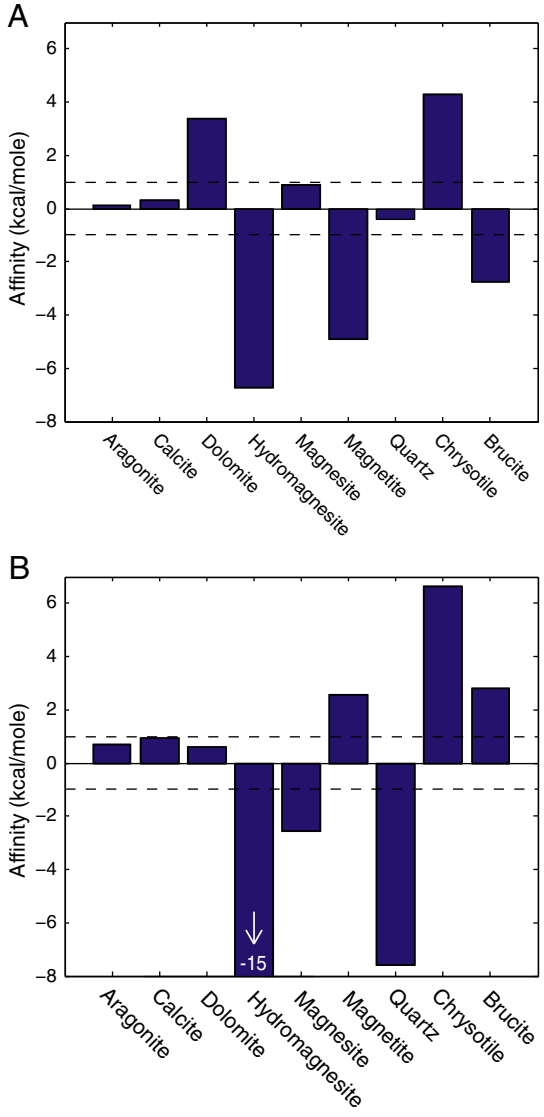

Fig. 3. Average saturation states for A) shallow groundwater samples, and B) alkaline spring water samples. Dashed lines indicate the affinity range in which the mineral is considered to be at saturation (+1 to −1 kcal/mole).

Table 3
Range in composition of mineral samples by depositional setting[a].

Depositional setting	Aragonite	Calcite	Brucite	Hydrated Mg-Carbonate
Crystalline film from spring water only	25–35	65–75	0	0
Crystalline film from mixed spring and surface water	55–96	1–45	1–3	0
Rippled terraces	40–100	0–60	0–7	0
Bottom floc	60–99	0–30	1–20	0
Misbit bottom floc	15–50	10–70	0–1	2–60

[a] All values in wt.%.

aeration, respectively. Our bottom floc also matches *Stanger's* gelatinous sediments of Ca-carbonate and brucite, which form in alkaline spring water and surface water mixing reactions.

There was one alkaline spring site which yielded unusual mineral samples: Misbit. Every sample from this location contained a hydrated Mg-carbonate, with the exception of the crystalline film atop the spring. Samples from Misbit were 40–98% calcium carbonate, 2–60% hydrated Mg-carbonate, and 0–1% brucite. The chemical composition of the hydrated Mg-carbonate has yet to be measured so the specific mineral is not known, but likely possibilities are hydrotalcite or pyroaurite. Unlike all of our other alkaline spring sites, Misbit lies in a catchment underlain by mixed peridotite and gabbro. The different rock composition may affect the chemistry of the groundwater and secondary mineral precipitation.

5. Reaction path model of the natural system

5.1. Model setup

In order to better understand the mechanisms of natural mineral carbonation in the peridotite of the Samail Ophiolite aquifer, a reaction path model was developed for the system. The model is based on that developed by Bruni et al. (2002) to model the reaction path between meteoric water and serpentinite in the Gruppo di Voltri, Italy. The Samail Ophiolite model presented in this paper adds reaction kinetics in order to predict the timescale required to develop the natural system.

The reaction path model was performed using EQ3/6, v.8.0 (Wolery and Jarek, 2003) and was designed to model water-rock interaction between meteoric water and peridotite under conditions mimicking the natural system. The reaction path model consists of two stages: an open system and a subsequent closed system. The open system input fluid represents rainwater recharge into a shallow aquifer. The fluid composition is the average of rainwater values for the mountains of northern Oman given in Weyhenmeyer (2000) (Table 4). The rainwater chemistry differs from what we might expect: if all rainwater solutes came from sea spray, their ratios should be the same as in seawater. However, the rainwater has excess Ca^{2+} and DIC relative to Na^+ and Cl^- levels, as well as elevated pH. The rainwater dataset is relatively limited, with only 7 samples. Dust may have settled on the collectors during dry periods prior to rain, altering the measured rainwater chemistry. Since the Samail Ophiolite is surrounded by $CaCO_3$-rich rocks – calcarenites and limestones in the underlying Hawasina Formation and marine limestones in the Arabian Platform Formation (Glennie et al., 1974) – the higher pH and extra Ca^{2+} and DIC are thought to be due to contamination of the rainwater samples by dissolution of $CaCO_3$ dust. It is likely that the recharge into the peridotite aquifer is similarly contaminated with $CaCO_3$ dust, so the rainwater composition is reasonable as the input fluid for the model.

The input water was introduced into the model and tracked as it interacted with peridotite in a system open to atmospheric exchange, with CO_2 and O_2 fugacities set to $10^{-3.4}$ and $10^{-0.7}$ bar, respectively.

Table 4
Input fluid — Oman rainwater[a].

Component	Concentration (mmol/l)
pH	6.6
Ca^{2+}	0.54
Na^+	0.37
Mg^{2+}	0.08
K^+	0.05
DIC	1.24
Cl^-	0.35
SO_4^{2-}	0.17
NO_3^-	0.10

[a] From Weyhenmeyer (2000).

The output water from the open system model then progressed to the closed system model, representing infiltration of shallow groundwater to a deeper, closed aquifer where the water continues to interact with peridotite, but with no further input of CO_2 or O_2.

Models were run using the fluid-centered flow-through physical system, as recommended by Bethke (1996) for tracing a parcel of water as it traverses an aquifer. As shown in Fig. 4, this means that the model follows the progress of 1 kg of water through its interaction with fresh peridotite and formation of secondary minerals. The available peridotite reservoir is unlimited, but fresh peridotite input is controlled by the dissolution kinetics of the primary minerals. After each reaction step, the amount of each secondary mineral that precipitated is tallied and those secondary minerals are removed from the equilibrium system so they cannot undergo any further reactions. The altered water then moves to the next step and encounters new peridotite. Models were run in reaction progress/time mode using dissolution kinetics to connect the two variables. The open system model was run for 50 years, by which time it had reached steady state. The closed system model was run until it reached pH 12, the maximum pH seen in the field, which required 6500 years.

The modeled peridotite is comprised of olivine (forsterite–fayalite solid solution), enstatite, and diopside. Spinel is also a primary mineral in peridotite of the Samail Ophiolite, but was not included in the model because field observations of relict spinels in otherwise altered peridotite indicate that spinel is commonly unaltered (Hanghoj et al., 2010). Halite was added as a primary mineral to produce the elevated levels of Na^+ and Cl^- seen in shallow groundwater and alkaline springs. The secondary minerals allowed to precipitate were limited to those seen in the field (Table 5). Consequently, magnesite and dolomite were suppressed in the open system but allowed to precipitate in the closed system. Unless otherwise specified, the temperature was 30 °C, which is the annual average temperature in the northern Oman mountains. All calculations were made with the standard YMP thermodynamic database provided with EQ3/6, v.8.0. The specific reactive surface area was set to a constant value of 0.26 cm^2/g for each mineral. This value was chosen because it corresponds to a reactive surface area for a "grain size" or fracture spacing of 0.7 m, the value used by Kelemen et al. (2011) for *in situ* mineral carbonation in peridotite.

Models were run using primary mineral dissolution kinetics, which are assumed to be the rate limiting step for both dissolution and secondary mineral precipitation. The dissolution rates for olivine (forsterite and fayalite) were calculated from empirically derived data found in Palandri and Kharaka (2004), enstatite from Oelkers and Schott (2001), and diopside from Knauss et al. (1993). All rates were taken from experiments at the temperatures closest to each of the model scenarios, and were adjusted by the model using the Arrhenius equation to match temperature conditions in each scenario (Table 6). The pH dependence of dissolution kinetics for each of the primary minerals was calculated using a power law regression on experimental dissolution data from pH ranges appropriate for each model — the open system used data from pH values up to 9, the closed system used data from pH values 9 to 12. Experimental dissolution rates for forsterite, fayalite, and diopside do not show pH dependence above pH9 (Palandri and Kharaka, 2004) and that is reflected in the closed system model kinetics. Average olivine in the Samail Ophiolite peridotite is a solid solution with 91% forsterite and 9% fayalite (Hanghoj et al., 2010), so forsterite and fayalite dissolution kinetics were modified to replicate this solid solution in the model. Rather than use a separately determined dissolution rate for fayalite, the fayalite rate was calculated by multiplying the olivine (Fo91) dissolution rate in Palandri and Kharaka (2004) by 0.09 to represent the 9% fayalite present. The forsterite rate was calculated by multiplying the olivine dissolution rate by 0.91 to represent the 91% forsterite present. Halite was added using a rate relative to the other primary minerals, not an actual kinetic rate. The relative number of moles was chosen so that the open system output water had a Cl^- concentration equal to the average for shallow

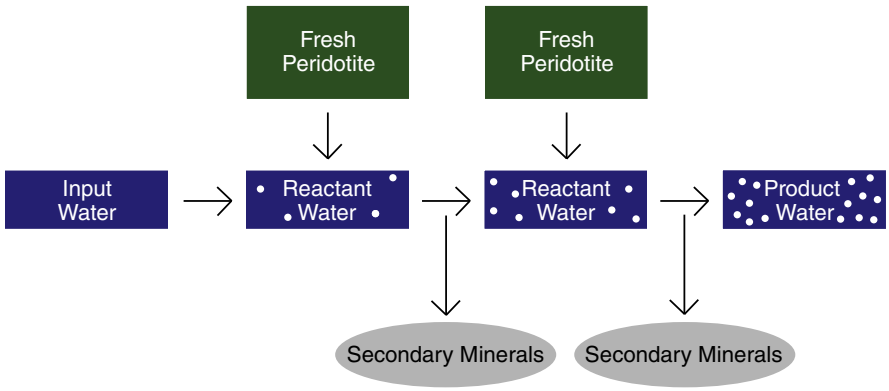

Fig. 4. Schematic for fluid-centered flow-through physical system model.

groundwater samples (3.5 mmol/l) and closed system output water had Cl^- concentration equal to the average for alkaline springs (7.25 mmol/l).

In the open system model, magnesite and dolomite precipitation were suppressed because field observations do not support their existence in the near-surface. Neither mineral is observed in areas around shallow groundwater. Additionally, if both minerals are allowed to precipitate in the open system, the modeled Mg^{2+} and DIC concentrations only reach half those measured in field samples. Magnesite and dolomite were allowed to precipitate in the closed system model because low temperature magnesite and dolomite are ubiquitous in veins in recent roadcuts and are also found in older outcrops throughout the Oman peridotite (Kelemen et al., 2011), suggesting that the minerals precipitate at depth.

5.2. Model results

The open system model attains steady state after 30 years. In order to reach this state, there is an increase in Mg^{2+}, Fe^{2+}, DIC, and pH, while $SiO_{2(aq)}$ and Ca^{2+} decrease (Fig. 5A). The dissolution of peridotite is compensated by precipitation of chrysotile, hydromagnesite, calcite, and magnetite (Fig. 5B). The resulting fluid has a Mg^{2+}-HCO_3^- composition.

The closed system model does not reach a stable aqueous composition. Fig. 5C shows an increase in, and eventual predominance, of Ca^{2+} and OH^- in solution. Fe^{2+}, and $SiO_{2(aq)}$ also increase, while Mg^{2+} decreases. pH initially decreases, then increases for the rest of the model. The dissolution of peridotite drives continual precipitation of chrysotile, brucite, and magnetite, and brief precipitation of a substantial quantity of magnesite, dolomite, calcite, and quartz, as well (Fig. 5D). Relatively early in the process, within the first 600 years, essentially all DIC disappears and carbonate precipitation ceases. Thus, it appears that the supply of inorganic C is the limiting factor in mineralization of CO_2 at depth, though it must be remembered that the model tracks a single parcel of water and does not allow mixing with ambient water, so there is no possibility of adding DIC through further infiltration from the shallow $Mg^{2+}-HCO_3^-$ aquifer.

After the cessation of carbonate precipitation, there are no mechanisms for Ca^{2+} removal from the fluid. With further peridotite dissolution, protons are consumed and Mg^{2+} is incorporated into brucite and chrysotile, while Ca^{2+} accumulates in the water. Ca^{2+} and OH^- concentrations continue to increase with time, so the final water composition has high Ca^{2+}, OH^- and pH, and virtually no Mg^{2+} or DIC.

At the beginning of the closed system model, large amounts of magnesite and dolomite form because they both were suppressed in the open system and became oversaturated. Unsuppressing them in the closed system allows them to precipitate, eliminating that oversaturation. This rapid formation of carbonates at the beginning of the closed system causes the pH to decrease from 8.9 to 7.9. After that initial pH drop, the pH begins to rise and continues to do so for the rest of the model.

Including precipitation kinetics in the closed system model would prolong the interval of magnesite and dolomite precipitation. For comparison, the model was run incorporating precipitation kinetics for magnesite, dolomite, and calcite (using the rate from Saldi et al. (2009) for both magnesite and dolomite, and Svensson and Dreybrodt (1992) for calcite), and suppressing all other carbonates. In the open system, the inclusion of precipitation kinetics prevents modeled concentrations of Mg^{2+} and DIC from ever reaching steady state, and after 50 years the concentrations of Mg^{2+} and DIC are double those seen in the field. In the closed system, inclusion of precipitation kinetics allows carbonate precipitation to continue for an additional 4000 years and for the storage of 15% more CO_2 in the form of carbonate minerals. This seems counterintuitive and is an artifact of the model: the inclusion of precipitation kinetics dramatically slows the rate of pH change, which affects redox conditions and consequently DIC concentration. In the closed system, the modeled DIC concentration drops precipitously when the Eh falls below the equilibrium line for $CO_3^{2-}-CH_4$ and most of the DIC converts to methane, preventing any further precipitation of carbonate minerals. Without precipitation kinetics, this occurs after approximately 600 years in the closed system. With precipitation kinetics, the model takes over 2000 years to become reducing enough to cross the

Table 5
Secondary minerals allowed to precipitate (unless otherwise specified).

Aragonite	Chrysotile
Calcite	Brucite
Dolomite	Amorphous Silica
Hydromagnesite	Quartz
Magnesite	Sepiolite
Magnetite	Nontronite
Greenalite	

Table 6
Primary mineral dissolution rates[a].

		Open System		Closed System		Eng. at 30 °C	Eng. at 90 °C
	E_A [b]	K at pH 0	nH^+	K at pH 9–12	nH^+	K at pH 3.5	K at pH 3.5
Forsterite	16.1	8.71E−09	0.28	2.40E−11	None	3.17E−09	7.43E−08[d]
Fayalite	16.1	8.61E−10	0.28	2.37E−12	None	3.14E−10	7.35E−09[d]
Enstatite	11.6	1.10E−09	0.25	8.24E−10[c]	0.24	1.46E−10	5.69E−09[e]
Diopside	9.7	3.16E−10	0.19	6.92E−12	None	6.78E−11	5.45E−10[f]

[a] All rates are in mol/m²/s. K refers to the rate at 25 °C unless otherwise specified. The models calculate K at the given temperatures assuming constant E_A. When rates are pH dependent, K refers to the rate at pH 0 and the model calcuates the rate for a given pH.
[b] Activation energies are given in kcal/mol.
[c] K refers to rate at pH 0.
[d] K refers to rate at 65 °C.
[e] K refers to rate at 100 °C.
[f] K refers to rate at 70 °C.

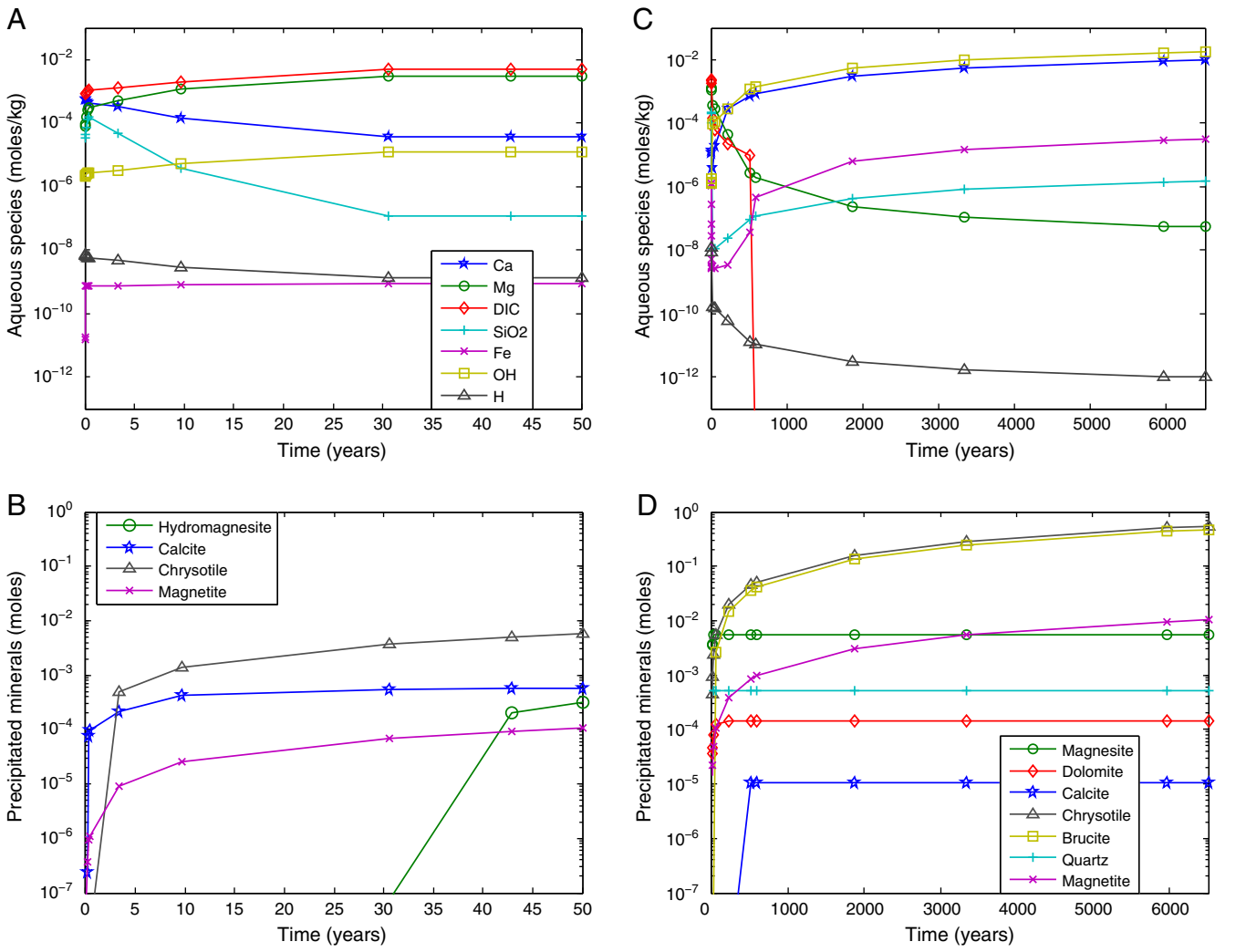

Fig. 5. A) Aqueous solutes in modeled fluids in the open system, B) cumulative secondary mineral precipitation in the open system, C) aqueous solutes in modeled fluids in the closed system, D) cumulative secondary mineral precipitation in the closed system. Data points are spaced at intervals of 1 log reaction progress and when there is a phase change in the equilibrium system.

$CO_3^{2-} - CH_4$ equilibrium line, and then it lingers near equilibrium for another 2000 years, so the interval of carbonate precipitation is much longer. Despite kinetic limitations, the much longer period of precipitation allows for the formation of slightly more carbonate minerals.

Though the effects of precipitation kinetics are interesting, they were not included in central model results because rates for precipitation of magnesite and dolomite at low temperature are not well-understood. In lab experiments at low temperature (<100 °C) and 1 bar pCO_2, Hänchen et al. (2008) saw no formation of magnesite, only the hydrated Mg-carbonates nesquehonite and hydromagnesite, so precipitation kinetics for magnesite at low temperature could not be calculated. Saldi et al. (2009) estimated the rate constant for magnesite at 25 °C from that measured at 100 °C, and calculated that even at 10× supersaturation the rate of magnesite precipitation is 6 orders of magnitude slower than that for calcite. Nonetheless, the existence of low temperature magnesite veins in the Samail Ophiolite (Kelemen et al., 2011; Streit et al., in press) demonstrates that there must be a mechanism for their formation. It is possible that magnesite precipitation took place in the form of a hydrated Mg-carbonate, such as hydromagnesite, which later dehydrated to form magnesite, as is seen in higher temperature lab experiments (Hänchen et al., 2008). Alternatively, the magnesite may have formed as a result of multiple cycles of alternating dissolution and precipitation of carbonates, in which each cycle forms progressively more stable phases like magnesite and dolomite and less metastable phases like dypingite and aragonite (Deelman, 1999; dos Anjos et al., 2011). Dolomite precipitation kinetics at low temperature are also poorly understood, despite years of study devoted to the "dolomite problem." Abiotic precipitation rates at low temperature, estimated from higher temperature experiments done by Arvidson and Mackenzie (1999), are 5 orders of magnitude slower than those for magnesite. Additionally, even after 32 years, Land (1998) saw no precipitation of dolomite from a solution with 1000× supersaturation with respect to dolomite. There may be biotic mechanisms responsible for catalyzing dolomite precipitation, such as sulfate reducing bacteria (e.g., Vasconcelos and McKenzie, 1997), but no estimates of microbial dolomite precipitation kinetics are available. Thus, given the uncertainty in magnesite and dolomite precipitation kinetics at relevant temperatures, precipitation kinetics for secondary minerals were not incorporated into the final version of the model (Fig. 5).

5.3. Comparing model results to field data — aqueous solute concentrations and saturation indices

In order to assess how well the model simulates natural *in situ* mineral carbonation in the Samail Ophiolite, the model results were compared to field data. The model shows rock–water mass transfer resulting in solute concentrations similar to those seen in the field (Fig. 6). Modeled trends in Mg^{2+} vs. pH fit within the range of sample

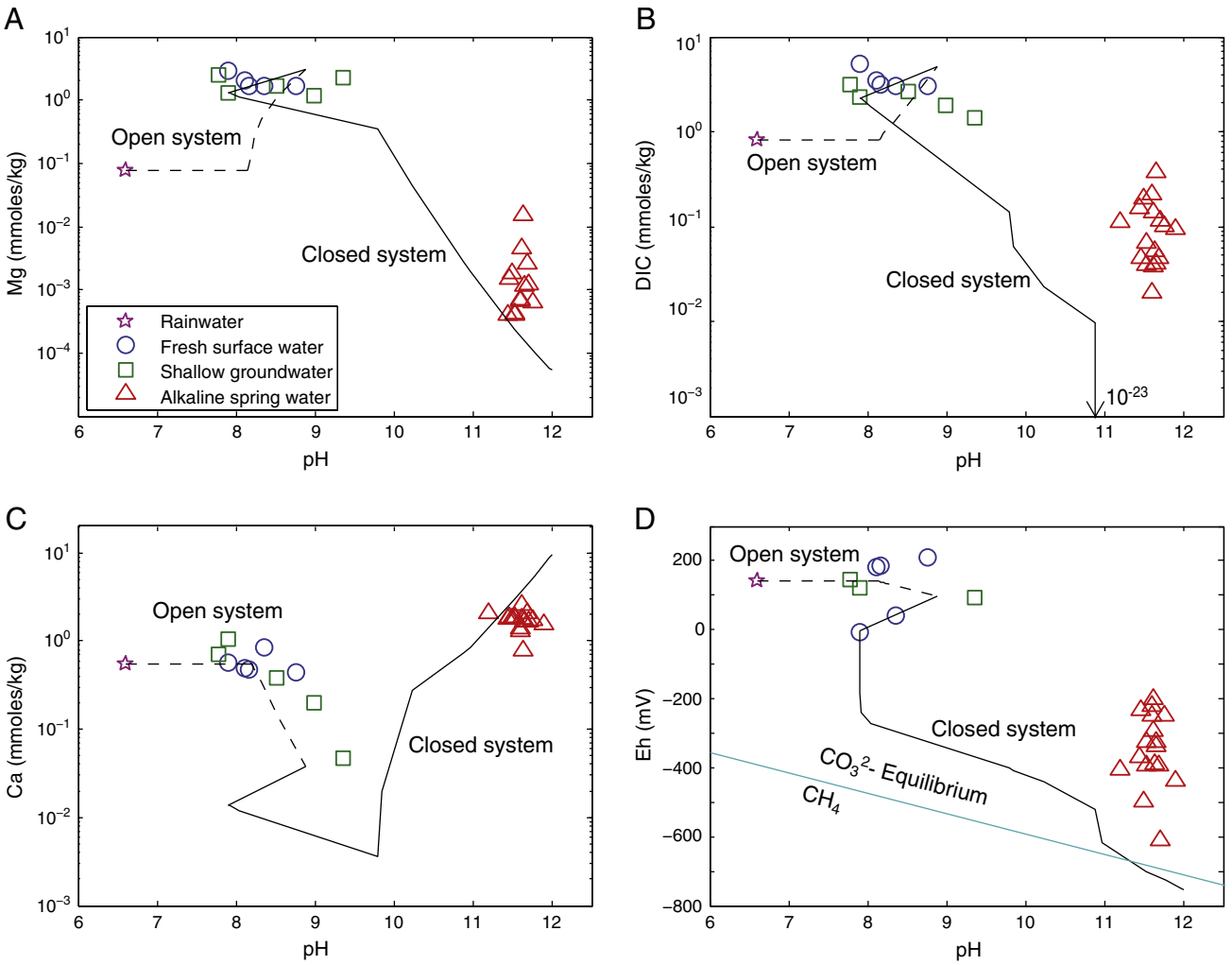

Fig. 6. Comparison between aqueous species in the modeled natural system and field samples during peridotite carbonation. A) Mg^{2+}, B) DIC, C) Ca^{2+}, D) Eh. Dashed line indicates model results along reaction progress in the open system. Solid line indicates model results along reaction progress in the closed system.

data. The Mg^{2+} concentration increases as the model progresses from neutral pH to pH 8.9, peaking at the end of the open system run, then the concentration decreases along the closed system flowpath to near zero values near the end of the model (Fig. 6A).

Modeled trends in DIC for the open system are similar to those seen in the field in surface and shallow groundwater, but in the closed system the DIC concentration decreases far below the values seen in alkaline springs (Fig. 6B). The steep decline in modeled DIC just before pH 11 is due to redox conditions dropping below the CO_3^{2-} – CH_4 equilibrium line and DIC converting to methane. This may not occur in the natural system, as alkaline spring waters are more oxidizing than the modeled water and all of our water samples lay above the methane equilibrium line on an Eh-pH diagram (Fig. 6D). The discrepancy between redox conditions in the model and the natural system are probably due to differences in incorporation of Fe into secondary minerals. In the natural alteration process, some Fe from olivine is incorporated into chrysotile in a solid solution with Mg^{2+} by different substitution mechanisms (Streit et al., in press). In the model, solid solutions are not allowed so Fe is excluded from chrysotile and is instead oxidized to form magnetite, consuming oxygen from the fluid. Thus, the model becomes more reducing than the natural system.

The modeled progression of Ca^{2+} captures trends seen in the natural system. The model starts with moderate Ca^{2+} concentration at neutral pH, then declines to low concentration as pH rises to 9.8, and finally increases again at high pH (Fig. 6C). However, there are minor discrepancies between the model and field samples. In the closed system model, Ca^{2+} concentrations rise steeply at high pH, reaching almost 10 mmol/l at pH 12, whereas in the field the highest Ca^{2+} concentrations are 2.5 mmol/l. It is possible that the spring waters had higher Ca^{2+} at depth, but they have lost Ca^{2+} due to precipitation of Ca-rich carbonates in the shallow subsurface due to either absorption of CO_2 in the vadose zone or mixing with CO_2-rich shallow groundwater. If this is the case, alkaline springs do not represent the actual endmember for the closed system, and it is possible that it has higher Ca^{2+} than the samples analyzed so far. Indeed, preliminary data from samples collected in the spring of 2012 from deep wells in the peridotite (up to 350 m depth) support this hypothesis.

Another method for evaluating how well the model approximates reaction processes in the natural system is to compare mineral saturation states produced in the model to those of actual water samples. Saturation states in the open system output water can be compared to those in shallow groundwater, while saturation states in the closed system output water can be compared to those in alkaline spring water. When comparing the saturation states of minerals in samples and models, it is important to remember that the model will not achieve oversaturation unless a mineral is suppressed. Unlike the real world, in the model there are no kinetic constraints on precipitation of secondary minerals, so precipitation proceeds as soon as saturation is reached. Therefore, an affinity of zero in a model can be considered equivalent to that of either saturation or oversaturation in a sample.

Fig. 7 gives the saturation states for model results. The modeled open system water is undersaturated with respect to brucite and quartz,

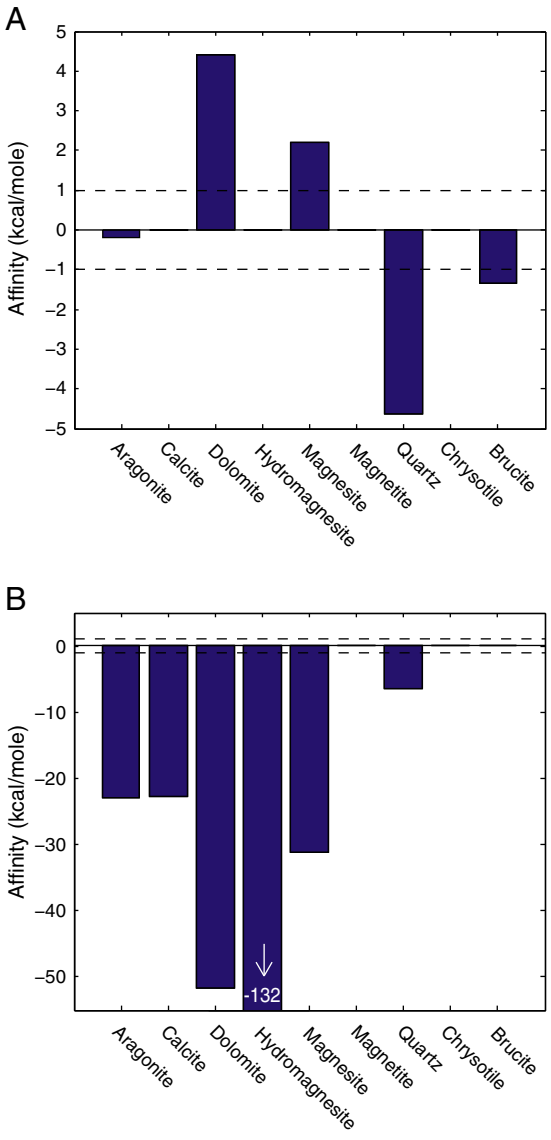

Fig. 7. Saturation states in the A) open system model, B) closed system model. Dashed lines indicate the affinity range in which the mineral is considered to be at saturation (+1 to −1 kcal/mole).

oversaturated with respect to dolomite and magnesite, and at saturation with respect to all other secondary minerals (Fig. 7A). The closed system water is saturated with respect to brucite, chrysotile, and magnetite, and undersaturated with respect to the other secondary minerals, including all carbonate species (Fig. 7B).

The saturation states for the open system agree with those of shallow groundwater samples for aragonite, calcite, dolomite, and brucite, but not for other secondary minerals. Chrysotile is at saturation in the model, but oversaturated in shallow groundwater. As noted above, this may be due to kinetic limitations on precipitation in the natural system. Quartz is undersaturated in the model but at saturation in the shallow groundwater. The ready precipitation of chrysotile in the model may also explain this discrepancy: in the model, chrysotile precipitation removes dissolved Si that would otherwise accumulate in the water, thus preventing quartz saturation from being reached. Magnetite is at saturation in the model, but undersaturated in shallow groundwater. As mentioned before, in the natural system, during peridotite alteration some of the Fe^{2+} released by olivine dissolution gets incorporated into serpentine (e.g., Streit et al., in press); however, the model does not allow this solid solution between Mg and Fe-serpentine so Fe accumulates in the water and eventually forms magnetite. Hydromagnesite is also at saturation in the model, but undersaturated in shallow groundwater. This may be because the shallow groundwater is at saturation with respect to magnesite. If the shallow groundwater is precipitating magnesite, then hydromagnesite should be undersaturated. As previously discussed, it remains an open question how the shallow groundwater precipitates magnesite at 30 °C when most lab experiments show no precipitation of magnesite at such low temperature. The interplay between magnesite, which is thermodynamically favored, and hydromagnesite, which is kinetically favored, is not yet understood.

The saturation states of minerals in the closed system water show similarities to those of alkaline spring water. Hydromagnesite, magnesite, and quartz are all undersaturated in both the model and alkaline spring water, though the level of undersaturation is much higher in the model. Brucite, chrysotile and magnetite are all oversaturated in alkaline spring water, and at saturation in in the model, again implying kinetic constraints on precipitation in the natural system. However, the Ca-rich carbonates- calcite, aragonite, and dolomite- are all at saturation in alkaline spring water but undersaturated in the model. The difference between the saturation state of Ca-rich carbonates in the field samples and in the closed system model may indicate that the spring water is not contained in a purely closed system until it reaches the surface. The modeled water is isolated from any sources of C and thus all carbonates remain undersaturated, but– as previously mentioned– prior to emerging, the spring water may have taken up CO_2 from the vadose zone or had contact with Mg^{2+} – HCO_3^- shallow groundwater, resulting in saturation or oversaturation of the Ca-rich carbonates (Neal and Stanger, 1985).

6. Reaction path modeling of CO_2 injection at 30 °C and 90 °C

6.1. Model setup

The Samail natural system model was expanded to include CO_2 injection scenarios at two temperatures: 30 °C and 90 °C. 30 °C is the annual average temperature in Oman, and 90 °C would be the expected temperature for an injection site at 2 km depth, assuming the average geothermal gradient. The model follows the approach of Cipolli et al. (2004) and Xu et al. (2004) for CO_2 injection into ultramafic rocks; however, there are some key differences between the *Cipolli* and *Xu* models and the Samail model developed for this paper. *Xu* modeled CO_2 injection into peridotite (forsterite and fayalite), but did not use the two-stage open system to closed system progression seen in alkaline spring water development. *Cipolli* did use the two-stage model, but simplified the serpentinite composition to be mono-mineralic and modeled CO_2 injection into Type II alkaline water by first modeling the open and closed systems and then fixing the CO_2 fugacity to 250 bar. The Samail Model equilibrates the product water from the open system with a CO_2 fugacity of 100 bar and uses that water as the input into the closed system. As in *Cipolli* and *Xu*, the constant supply of CO_2 from injection is simulated by maintaining a fixed CO_2 fugacity throughout the model, meaning that at the beginning of each step of reaction progress, the water reequilibrates with 100 bar pCO_2 and then that CO_2 saturated water reacts with new peridotite. The model does not consider reactions between the CO_2 gas phase and the rock. Primary mineral dissolution kinetics for each CO_2 injection scenario are given in Table 6. Neither engineered system incorporates pH dependence into dissolution kinetics because at each reaction step when the water reequilibrates with 100 bar pCO_2, the pH drops back to 3.5. Both CO_2 injection models run for 30 years, which is considered to be a reasonable lifetime for a CO_2 injection project.

6.2. Model results

In both engineered systems, most aqueous species achieve steady state concentrations within 5 years, though in the lower temperature model the Fe and Ca^{2+} concentrations continue to increase until the

end of the model at 30 years (Fig. 8A and C). Both models show precipitation of carbonate minerals throughout the injection period. Most secondary mineral formation is in the form of magnesite and quartz with minor magnetite, and the 90 °C system has additional dolomite (Fig. 8B and D).

The change from precipitation of chrysotile and brucite in the natural closed system to magnesite and quartz in the CO_2 injection systems fits the expected shift in alteration products at higher pCO_2 (e.g., Figs. 1 and 2 in Kelemen et al. (2011)). Hansen et al. (2005) suggested an alteration succession that occurs with increasing levels of CO_2, generating progressively more magnesite: when olivine is combined with water and CO_2, it alters to antigorite and magnesite, and sometimes brucite. With more CO_2, the antigorite converts to talc and magnesite, and the brucite converts to magnesite. Finally, with even more CO_2, the talc alters to magnesite and quartz, making the final products only magnesite and quartz. Thus, the Samail reaction path models predict a similar progression of alteration products for peridotite carbonation to that seen by Hansen et al. in the serpentinite carbonation front.

6.3. Enhanced CO_2 mineralization

The fact that inorganic C is a limiting factor in the natural system suggests one could enhance mineralization by increasing the supply of CO_2 to the system, and the engineered system models corroborate this. Fig. 9 tracks the amount of CO_2 sequestered as carbonate minerals for each of the closed system models. The engineered model at 30 °C indicates that maintaining a CO_2 fugacity of 100 bar would result in about a 200× increase in the amount of CO_2 sequestered in 30 years relative to the natural system, that is, a 200× increase in the rate of CO_2 mineralization.

In addition to increasing CO_2 availability, increasing temperature was tested as another method for enhancing CO_2 mineralization. The engineered model at 90 °C indicates that raising the temperature by 60 °C would result in a 76x increase in the amount of CO_2 sequestered over the CO_2 injection system at 30 °C. This makes the total amount of CO_2 sequestration in the 90 °C engineered CO_2 injection scenario about 16,000 times the amount sequestered by the natural system over the same time frame. This rate enhancement is approximately 10 times greater than that predicted using Kelemen and Matter (2008) Eq. (4), based on the rate from experimental results of O'Connor et al. (2004) for olivine carbonation at a variety of temperatures and pCO_2 in aqueous solutions with 1 M NaCl an 0.64 M $NaHCO_3$.

In addition to increasing the total amount of CO_2 mineralized, CO_2 injection also increases the efficiency of peridotite carbonation. Table 7 compares the amount of peridotite consumed with the amount of CO_2 sequestered over the course of the model. The CO_2/peridotite mass ratios show an increase of over 350× in mineralization efficiency in the enhanced processes. Given that complete carbonation of forsterite

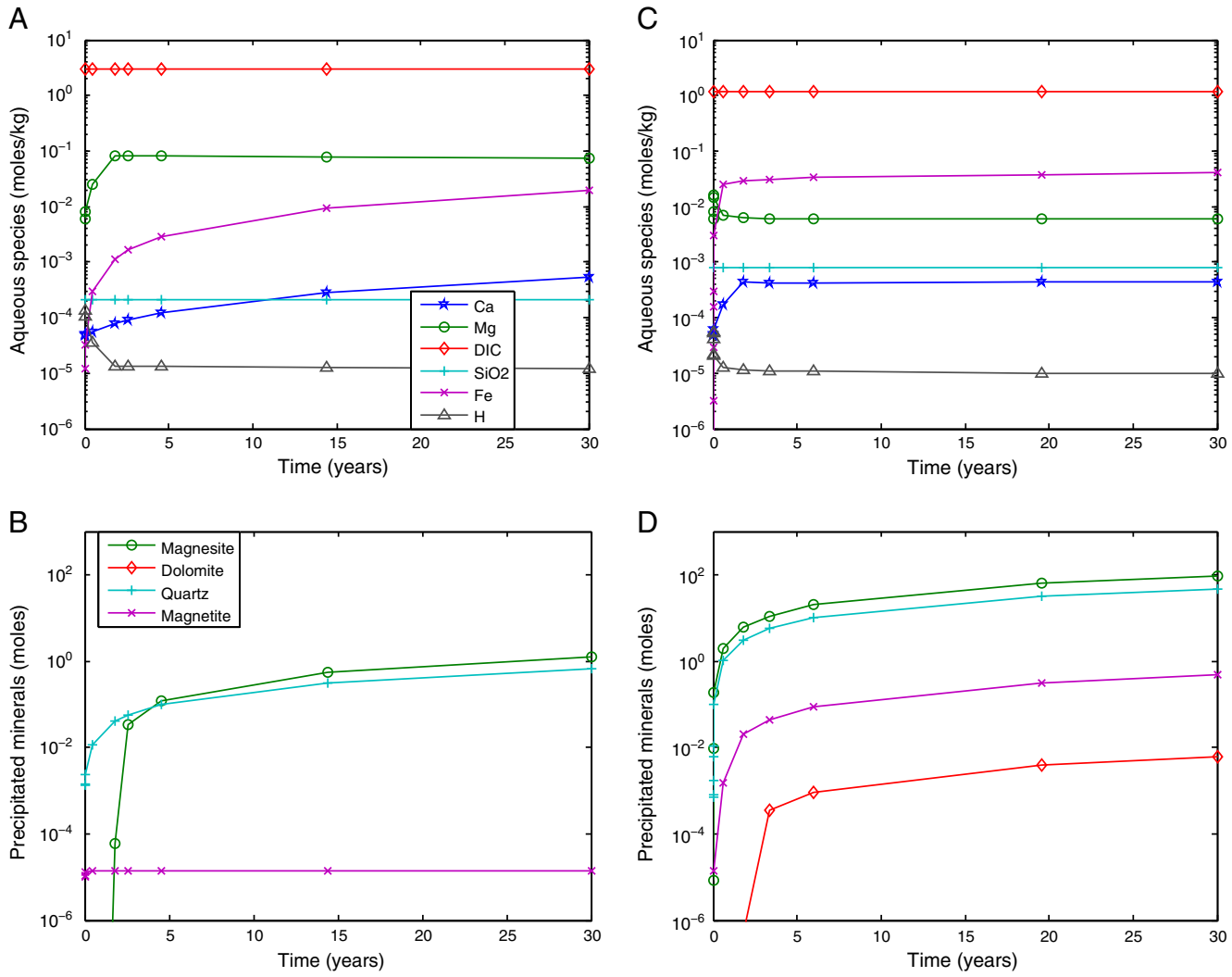

Fig. 8. Results from models with CO_2 injection at 100 bar pCO_2 : A) aqueous solutes in modeled fluids at 30 °C, B) cumulative secondary mineral precipitation at 30 °C, C) aqueous solutes in modeled fluids at 90 °C, D) cumulative secondary mineral precipitation at 90 °C. Data points are spaced at intervals of 1 log reaction progress and when there is a phase change in the equilibrium system.

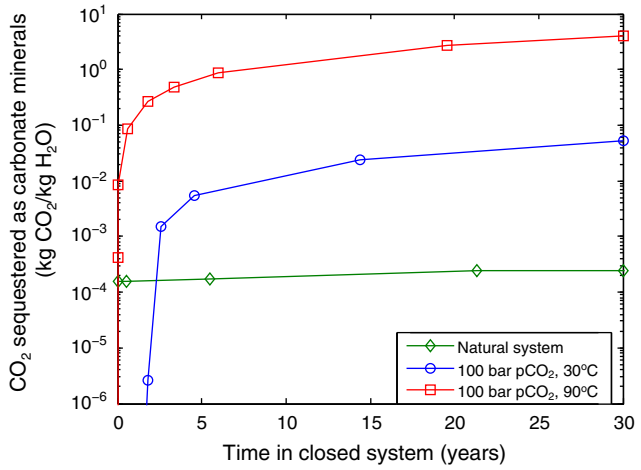

Fig. 9. Cumulative amount of CO_2 sequestered in the form of carbonate minerals in each of the closed system models: the natural system, CO_2 injection at 30 °C and CO_2 injection at 90 °C. Data points are spaced at intervals of 1 log reaction progress and when there is a phase change in the equilibrium system.

would result in a CO_2/peridotite ratio of 0.63, the ratio of 0.61 in the 90 °C CO_2 injection scenario indicates almost complete carbonation.

The reasons for the increase in CO_2 mineralization rate and efficiency are three-fold. First, since CO_2 availability limits the amount of CO_2 sequestered at depth in the natural system, CO_2 injection changes the limiting factor in mineralization by drastically increasing CO_2 availability. Secondly, CO_2 injection lowers the pH of the fluid from 9 to 3.5, which increases the dissolution kinetics for primary minerals by a factor of between 10 and 130 (Table 6). Thirdly, in the 90 °C case, the increase in temperature results in another acceleration of dissolution kinetics by a factor of between 8 and 40 (Table 6).

All models show a positive volume increase, ranging from 45-50% in the natural system to almost 80% in the CO_2 injection scenario at 90 °C (Table 7). This volume increase due to serpentinization and carbonation of peridotite will have to be taken into account when considering long-term injectivity into a fractured peridotite aquifer, as the secondary minerals could clog the pores and pathways, preventing further injection. The precipitation of carbonate minerals on the fracture walls might protect the underlying peridotite from further reaction. Armoring of the olivine by a silica-rich passivating layer, such as that seen in laboratory experiments conducted by Andreani et al. (2009), could also reduce the amount of peridotite available to react. Alternatively, the volume increase could cause reactive cracking, which would open new fractures and could help maintain permeability and porosity (Fletcher et al., 2006; Kelemen and Matter, 2008; Jamtveit et al., 2008; Rudge et al., 2010; Kelemen et al., 2011; Jamtveit et al., 2011; Kelemen and Hirth, 2012).

7. Model uncertainties and limitations

It should be noted that the models discussed in this paper provide a limited view of CO_2 mineralization in peridotite due to exclusion of important factors, such as hydrologic parameters for the system. EQ6 modeling cannot consider the effects of permeability, porosity, or injectivity, which may be crucial — particularly in fractured rock aquifers with low permeability and porosity. While the models provide estimates of volume increases due to secondary mineralization, these increases do not feed back onto permeability or porosity: the model ignores both negative feedbacks due to diminished permeability and armoring of reactive surfaces, and positive feedbacks due to reaction-driven cracking.

Another limitation of the models is their simplification of reaction kinetics. The models assume that dissolution of primary minerals is the rate-limiting step, but this may not always be the case (particularly with regard to precipitation of magnesite and dolomite). Reaction kinetics are further simplified by assuming a constant specific reactive surface area. In a porosity regime dominated by fractures, such as that expected in the Samail Ophiolite aquifer, the reactive surface area can be assumed to be the amount of rock exposed to fluid by fractures. It is difficult to estimate the starting value for this reactive surface area, and the value used in the model is probably a considerable underestimate. The 0.7 m fracture spacing used in this model may be reasonable for large scale fractures; however, altered peridotite of the Samail Ophiolite shows fractures down to the 10 μm scale (Kelemen et al., 2011). Closer fracture spacing could dramatically increase the reactive surface area, which would cause a comparable increase in dissolution rate because the two factors scale linearly. The uncertainty in reactive surface area is compounded by the fact that it doubtless changes over the course of the reaction.

A reactive transport model incorporating local hydrology and changes in reactive surface area, porosity, and permeability over the course of the mineral carbonation process could provide a more complete picture of both natural CO_2 mineralization in the Samail Ophiolite and the effects of and limitations to enhancing the process, and will be pursued as a next step.

8. Conclusions

- The natural system model provides a useful representation of the evolution of water in the peridotite aquifers of the Samail Ophiolite: from surface water, to shallow $Mg^{2+}-HCO_3^-$ water, to deep alkaline $Ca^{2+}-OH^-$ water.
- The open system model is characterized by precipitation of hydromagnesite, calcite, chrysotile, and magnetite, while the closed system model is characterized by precipitation of chrysotile, brucite and magnetite, with a brief period of abundant magnesite, dolomite, and calcite precipitation in the initial stages of reaction progress.
- The open system model reaches steady state within a few decades, while the closed system model continues to evolve with time, taking 6500 years to reach the upper extent of pH seen in field samples.
- The amount of CO_2 mineralization in the natural system at depth, where it is isolated from CO_2 uptake from the atmosphere, is limited by the dissolved inorganic C concentration in the incoming $Mg^{2+}-HCO_3^-$ groundwater, as seen in the closed system natural model.
- Injecting CO_2 to maintain a constant fugacity of 100 bar could increase the amount of CO_2 mineralized in 30 years by a factor of over 200.
- Increasing the temperature of a CO_2 injection system from 30 °C to 90 °C could increase the CO_2 sequestered by another factor of over

Table 7
Peridotite consumption, CO_2 mineralization, and volume change in each model scenario.

Model scenario	Peridotite consumed (kg)	CO_2 sequestered (kg)	CO_2/Peridotite mass ratio	Peridotite consumed (cm^3)	Secondary minerals formed (cm^3)	Volume change (%)
Natural open system	1.61E−03	8.17E−05	5.1E−02	0.5	0.7	44.9
Natural closed system	1.55E−01	2.54E−04	1.6E−03	47.8	72.1	50.7
30 °C, 100 bar pCO_2	9.29E−02	5.37E−02	0.58	28.7	49.2	71.0
90 °C, 100 bar pCO_2	6.72	4.11	0.61	2078.0	3711.9	78.6
Complete carbonation	1.00	0.63	0.63			

75, giving a total rate enhancement of over 16,000 times that in the natural system.
- CO_2 injection at 100 bar pCO_2 increases the efficiency of carbonation by 350–370 times, to the point of near-complete carbonation, and hence would allow significantly more CO_2 to be mineralized in the same volume of peridotite.

Acknowledgments

We would like to extend special thanks for their generosity to everyone at the Ministry of Regional Municipalities and Water Resources, Sultanate of Oman, particularly Salim Al Khanbashi and Dr. Abdulaziz Ali-AL-Mashikhi, and everyone at the Geological Survey of Oman and the Directorate General of Minerals in the Ministry of Commerce and Industry, particularly Dr. Ali Al Rajhi and Dr. Salim Al Busaidi. We thank Lisa Streit, Peter Canovas, Evelyn Mervine, and Alison Keimowitz for help during the 2009–2011 field seasons, and Martin Stute for advice in the lab. This work was supported through the NSF Graduate Research Fellowship Program, Columbia Research Initiative in Science and Engineering, Lamont-Doherty Earth Observatory, Petroleum Development Oman, NSF Research Grant MGG-1059175, and Kelemen's Arthur D. Storke Chair at Columbia University. Kelemen's contribution was supported by NSF Research Grant EAR-1049905 and the Storke Chair.

References

Andreani, M., Luquot, L., Gouze, P., Godard, M., Hoise, E., Gibert, B., 2009. Experimental study of carbon sequestration reactions controlled by the percolation of CO_2-rich brine through peridotites. Environmental Science & Technology 43, 1226–1231.

Arvidson, R.S., Mackenzie, F.T., 1999. The dolomite problem: control of precipitation kinetics by temperature and saturation state. American Journal of Science 299, 257–288.

Barnes, I., O'Neil, J., 1969. The relationship between fluids in some fresh alpine-type ultramafics and possible modern serpentinization, Western United States. Geological Society of America Bulletin 80, 1947–1960.

Benson, S.M., Cook, P., Anderson, J., Bachu, S., Nimir, H.B., Basu, B., Bradshaw, J., Deguchi, G., Gale, J., von Goerne, G., Heidug, W., Holloway, S., Kamal, R., Keith, D., Lloyd, P., Rocha, P., Senior, B., Thomson, J., Torp, T., Wildenborg, T., Wilson, M., Zarlenga, F., Zhou, D., Celia, S.M., Gunter, B., Ennis King, J., Lindegerg, E., Lombardi, S., Oldenburg, C., Pruess, K., Rigg, A., Stevens, S., Wilson, E., Whittaker, S., 2005. Underground geological storage. In: Metz, B., Davidson, O., de Coninck, H., Loos, M., Meyer, L. (Eds.), IPCC Special Report on Carbon Dioxide Capture and Storage. Cambridge University Press, Cambridge, UK.

Bethke, C.M., 1996. Modeling Overview. Geochemical Reaction Modeling. Oxford University Press, New York, NY, p. 19.

Boudier, F., Coleman, R.G., 1981. Cross section through the peridotite in the samail ophiolite, Southeastern Oman mountains. Journal of Geophysical Research 86 (B4), 2573–2592.

Bruni, J., Canepa, M., Chiodini, G., Cioni, R., Cipolli, F., Longinelli, A., Marini, L., Ottonello, G., Zuccolini, M.V., 2002. Irreversible water-rock mass transfer accompanying the generation of the neutral, $Mg-HCO_3$ and high-pH, $Ca-OH$ spring waters of the Genova province, Italy. Applied Geochemistry 17, 455–474.

Burns, S.J., Matter, A., 1995. Geochemistry of carbonate cements in surficial alluvial conglomerates and their paleoclimatic implications, Sultanate of Oman. Journal of Sedimentary Research 65 (1a), 170–177.

Chadwick, R.A., Zweigel, P., Gregersen, U., Kirby, G.A., Holloway, S., Johannessen, P.N., 2004. Geological reservoir characterization of a CO2 storage site: the Utsira Sand, Sleipner, Northern North Sea. Energy 29, 1371–1381.

Chizmeshya, A.V.G., McKelvy, M.J., Squires, K., Carpenter, R.W., Bearat, H., 2007. DOE Final Report 924162: A novel approach to mineral carbonation: Enhancing carbonation while avoiding mineral pretreatment process cost.

Cipolli, F., Gambardella, B., Marini, L., Ottonello, G., Zuccolini, M.V., 2004. Geochemistry of high-pH waters from serpentinites of the Gruppo di Voltri (Genova, Italy) and reaction path modeling of CO_2 sequestration in serpentinite aquifers. Applied Geochemistry 19, 787–802.

Clark, I.D., Fontes, J.C., 1990. Paleoclimatic reconstruction in northern Oman based on carbonates from hyperalkaline groundwaters. Quaternary Research 33 (3), 320–336.

Deelman, J.C., 1999. Low-temperature nucleation of magnesite and dolomite. Neues Jahrbuch für Mineralogie, Monatshefte 7, 289–302.

Dewandel, B., Lachassagne, P., Boudier, F., Al-Hattali, S., Ladouche, B., Pinault, J.-L., Al-Suleimani, Z., 2005. A conceptual hydrogeological model of ophiolite hard-rock aquifers in Oman based on a multiscale and a multidisciplinary approach. Hydrogeology Journal 13, 708–726.

dos Anjos, A.P.A., Sifeddine, A., Sanders, C.J., Patchineelam, S.R., 2011. Synthesis of magnesite at low temperature. Carbonates and Evaporites 26, 213–215.

Fletcher, R.C., Buss, H.L., Brantley, S.L., 2006. A spheroidal weathering model coupling porewater chemistry to soil thickness during steady-state denudation. Earth and Planetary Science Letters 244 (1–2), 444–457.

Giammar, D.E., Bruant Jr., R.G., Peters, C.A., 2005. Forsterite dissolution and magnesite precipitation at conditions relevant for deep saline aquifer storage and sequestration of carbon dioxide. Chemical Geology 217, 257–276.

Gislason, S.R., Eugster, P.H., 1987. Meteoric water-basalt interactions. I: A laboratory study. Geochimica et Cosmochimica Acta 51 (10), 2827–2840.

Glennie, K.W., Boeuf, M.G.A., Hughes Clarke, M.W., Moody-Stuart, M., Pilaar, W.F.H., Reinhardt, B.M., 1974. Geology of the Oman Mountains.

Gysi, A.P., Stefansson, A., 2011. CO_2-water-basalt interaction. Numerical simulation of low temperature CO_2 sequestration into basalts. Geochim. Cosmochim. Geochimica et Cosmochimica Acta 75, 4728–4751.

Hänchen, M., Prigiobbe, V., Storti, G., Seward, T.M., Mazzotti, M., 2006. Dissolution kinetics of forsteritic olivine at 90–150 °C including effects of the presence of CO2. Geochimica et Cosmochimica Acta 70, 4403–4416.

Hänchen, M., Prigiobbe, V., Baciocchi, R., Mazzotti, M., 2008. Precipitation in the Mg-carbonate system — effects of temperature and CO_2 pressure. Chemical Engineering Science 63, 1012–1028.

Hanghoj, K., Kelemen, P., Hassler, D., Godard, M., 2010. Composition and genesis of depleted mantle peridotites from the Wadi Tayin Massif, Oman Ophiolite; major and trace element geochemistry, and Os isotope and PGE systematics. Journal of Petrology 51 (1–2), 201–227.

Hansen, L.D., Dipple, G.M., Gordon, T.M., Kellett, D.A., 2005. Carbonated serpentinite (Listwanite) at Atlin, British Columbia: a geological analogue to carbon dioxide sequestration. The Canadian Mineralogist 43 (1), 225–239.

Holloway, S., 2005. Underground sequestration of carbon dioxide — a viable greenhouse gas mitigation option. Energy 30, 2318–2333.

Jamtveit, B., Malthe-Sorenssen, A., Kostenko, O., 2008. Reaction enhanced permeability during retrograde metamorphism. Earth and Planetary Science Letters 267 (3–4), 620–627.

Jamtveit, B., Kobchenko, M., Austrheim, H., Malthe-Sorenssen, A., Royne, A., Svensen, H., 2011. Porosity evolution and crystallization-driven fragmentation during weathering of andesite. Journal of Geophysical Research 116, B12204.

Kelemen, P.B., Hirth, G., 2012. Reaction-driven cracking during retrograde metamorphism: Olivine hydration and carbonation. Earth and Planetary Science Letters 345–348, 81–89.

Kelemen, P., Matter, J., 2008. In situ carbonation of peridotite for CO_2 storage. Proceedings of the National Academy of Sciences 11 (45), 17295–17300.

Kelemen, P.B., Matter, J.M., Streit, E.E., Rudge, J.F., Curry, W.B., Blusztajn, J., 2011. Rates and mechanisms of mineral carbonation in peridotite: natural processes and recipes for enhanced, in situ CO_2 capture and storage. Annual Review of Earth and Planetary Sciences 39, 545–576.

Knauss, K.G., Nguyen, S.N., Weed, H.C., 1993. Diopside dissolution kinetics as a function of pH, C02, temperature, and time. Geochimica et Cosmochimica Acta 57, 285–294.

Land, L.S., 1998. Failure to precipitate dolomite at 25 °C from dilute solution despite 1000-fold oversaturation after 32 years. Aquatic Geochemistry 4, 361–368.

Lutterotti, L., Matthies, S., Wenk, H.-R., Schultz, A.S., Richardson, J.W., 1997. Combined texture and structure analysis of deformed limestone from time-of-flight neutron diffraction spectra. Journal of Applied Physics 81 (2), 594–600.

Matter, J.M., Kelemen, P.B., 2009. Permanent storage of carbon dioxide in geological reservoirs by mineral carbonation. Nature Geoscience 2, 837–841.

Matter, J., Takahashi, T., Goldberg, D., 2007. Experimental evaluation of in situ CO2-water-rock reaction during CO2 injection in basaltic rocks: implications for geological CO2 sequestration. Geochemistry, Geophysics, Geosystems 8 (2), 1–19.

Mazzotti, M., Abanades, J.C., Allam, R., Lackner, K.S., Meunier, F., Rubin, E., Sanchez, J.C., Yogo, K., Zevenhoven, R., 2005. Mineral carbonation and industrial uses of carbon dioxide. In: Metz, B., Davidson, O., de Coninck, H., Loos, M., Meyer, L. (Eds.), IPCC Special Report on Carbon Dioxide Capture and Storage. Cambridge University Press, Cambridge, UK.

McCollom, T.M., Bach, W., 2009. Thermodynamic constraints on hydrogen generation during serpentinization of ultramafic rocks. Geochimica et Cosmochimica Acta 73, 856–875.

McGrail, B.P., Schaef, H.T., Ho, A.M., Chien, Y.J., Dooley, J.J., Davidson, C.L., 2006. Potential for carbon dioxide sequestration in flood basalts. Journal of Geophysical Research 111, 1–13.

Neal, C., Stanger, G., 1985. Past and Present Serpentinisation of Ultramafic Rocks: An Example from the Semail Ophiolite Nappe of Northern Oman. In: Drever, J.I. (Ed.), The Chem. of Weathering. Reidel Publishing Company, Dordrecht, Holland, pp. 249–275.

Nicolas, A., Boudier, E., Ildefonse, B., Ball, E., 2000. Accretion of Oman and United Arab Emirates ophiolite: discussion of a new structural map. Marine Geophysical Researches 21 (3–4), 147–179.

O'Connor, W.K., Dahlin, D.C., Rush, G.E., Gerdemann, S.J., Nilsen, D.N., 2004. Final report: Aqueous mineral carbonation . DOE/ARC-TR-04-002 .

Oelkers, E.H., 2001. An experimental study of forsterite dissolution rates as a function of temperature and aqueous Mg and Si concentrations. Chemical Geology 175, 485–494.

Oelkers, E.H., Schott, J., 2001. An experimental study of enstatite dissolution rates as a function of pH, temperature, and aqueous Mg and Si concentration, and the mechanism of pyroxene/pyroxenoid dissolution. Geochimica et Cosmochimica Acta 65 (8), 1219–1231.

Oelkers, E.H., Gislason, S.R., Matter, J., 2008. Mineral carbonation of CO2. Elements 4, 333–337.

Orberger, B., Friedrich, G., Woermann, E., 1990. The distribution of halogens and carbon in PGE-bearing ultramafics of the Acoje ophiolite block, Zambales, Philippines. Journal of Geochemical Exploration 37, 147–169.

Palandri, J.L., Kharaka, Y.K., 2004. A Compilation of Rate Parameters of Water-Mineral Interaction Kinetics for Application to Geochemical Modeling . USGS. Open File Report 2004-1068.

Rudge, J.F., Kelemen, P.B., Spiegelman, M., 2010. A simple model of reaction-induced cracking applied to serpentinization and carbonation of peridotite. Earth and Planetary Science Letters 291, 215–227.

Saar, M.O., Manga, M., 1999. Permeability-porosity relationship in vesicular basalts. Geophysical Research Letters 26 (1), 111–114.

Saldi, G.D., Jordan, G., Schott, J., Oelkers, E.H., 2009. Magnesite growth rates as a function of temperature and saturation state. Geochimica et Cosmochimica Acta 73 (19), 5646–5657.

Schaef, H.T., McGrail, B.P., 2009. Dissolution of Columbia River Basalt under mildly acidic conditions as a function of temperature: experimental results relevant to the geological sequestration of carbon dioxide. Applied Geochemistry 24, 980–987.

Seifritz, W., 1990. CO_2 disposal by means of silicates. Nature 345 (6275), 486.

Sharp, Z.D., Barnes, J.D., 2004. Water-soluble chlorides in massive seafloor serpentinites: a source of chloride in subduction zones. Earth and Planetary Science Letters 226, 243–254.

Stanger, G., 1986. The hydrogeology of the Oman Mountains. PhD Thesis, Open University London, UK.

Streit, E., Kelemen, P., Eiler, J., in press. Coexisting serpentine and quartz from carbonate-bearing serpentinized peridotite in the Samail Ophiolite, Oman. Contributions to Mineralogy and Petrology. http://dx.doi.org/10.1007/s00410-012-0775-z.

Svensson, U., Dreybrodt, W., 1992. Dissolution kinetics of natural calcite minerals in CO_2–water systems approaching calcite equilibrium. Chemical Geology 100, 129–145.

Vasconcelos, C., McKenzie, J.A., 1997. Microbial mediation of modern dolomite precipitation and diagenesis under anoxic conditions (Lagoa Vermelha, Rio De Janeiro, Brazil). Journal of Sedimentary Petrology 67, 378–390.

Weyhenmeyer, C., 2000. Origin and evolution of groundwaters in the alluvial aquifer of the Eastern Batinah Coastal Plain, Sultanate of Oman. PhD Thesis, University of Bern, Switzerland.

White, A.F., Brantley, S.L., 2003. The effect of time on the weathering of silicate minerals: why do weathering rates differ in the laboratory and field? Chemical Geology 202, 479–506.

Wolery, T.W., Jarek, R.L., 2003. Software User's Manual EQ3/6, Version 8.0. Software Document Number 10813-UM-8.0-00 Sandia National Lab.

Wolff-Boenisch, D., Wenau, S., Gislason, S.R., Oelkers, E.H., 2011. Dissolution of basalts and peridotite in seawater, in the presence of ligands, and CO_2: implications for mineral sequestration of carbon dioxide. Geochimica et Cosmochimica Acta 75, 5510–5525.

Xu, T., Apps, J.A., Pruess, K., 2004. Numerical simulation of CO_2 disposal by mineral trapping in deep aquifers. Applied Geochemistry 19, 917–936.